Check for updates

One-pot synthesis of NiFe nanoarrays under an external magnetic field as an efficient oxygen evolution reaction catalyst†

Yujie Miao,[a] Qiuping Huang,[a] Dan Wen,[a] Dongling Xie,[a] Bo Huang,[a] Dunmin Lin, [ID][a] Chenggang Xu,[a] Wen Zeng [ID][b] and Fengyu Xie [ID]*[a]

Designing and developing earth-abundant electrocatalysts for the oxygen evolution reaction (OER) in alkaline media is a critical element in the societal development of sustainable energy. MIL-53(Fe–Ni)/NF-2200Gs was synthesized under an external magnetic field. Such MIL-53(Fe–Ni)/NF-2200Gs show exceptionally high catalytic activity and require an overpotential of only 174 mV to drive a geometrical catalytic current density of 10 mA cm^{-2} in 1.0 M KOH, superior to RuO_2 and most Fe, Ni-based electrocatalysts. Our work emphasizes the optimization of catalytic activity originating from the improvement of the magnetic properties of the catalyst, which enhances the spin polarization and tailors the d-electron structure of cations, leading to outstanding OER activity. This work would open new opportunities to design and develop transition-metal-based nanometer arrays toward efficient and stable water oxidation in alkaline media for applications.

The increased environmental pollution and shortage of fossil fuels have spurred an urgent demand to develop alternative clean energy. As a promising energy carrier for replacing fossil fuels, hydrogen processes involve high gravimetric energy density and do not emit contaminants and carbon dioxide, unlike alkaline water electrolysis technology.[1–3] One of the essential tasks for such an application is the development of highly active electrocatalysts for the oxygen evolution reaction (OER), which suffers from natural slow kinetics and high overpotential owing to the proton-electron transfer step.[4–6]

The optimization of the electronic structure of the catalyst has been previously reported to positively affect OER. In 1848, Faraday discovered that the oxygen molecule is paramagnetic. Therefore, from H_2O/OH^- to O_2 (OER), the reactions involving triplet oxygen (↑O═O↑) are related to spin-related electron transfer, which plays a considerable role in the reaction kinetics.[7–10] Thus far, substantial research has shown that explicit spin selection of ferromagnetic OER catalysts can reduce the kinetic barrier to promote OER in alkaline conditions.[11–15] The motion of paramagnetic species is caused by the Kelvin force, which can be enhanced by embedding ferromagnetic catalysts in the electrode. According to the above reasons, magnetization improves spin polarization in materials,

which should be in a preferred path to obtain the foremost OER catalysts. It is well known that Fe and Ni are magnetic ions, and their complex has excellent OER catalytic activity.[16–20] Unfortunately, from a broader perspective, the role of magnetism in the compounds of Fe and Ni in increasing their OER activity is still underestimated.

Herein, we synthesized MIL-53(Fe–Ni) nanosheet arrays on a nickel foam (MIL-53(Fe–Ni)/NF) using one-step solvent thermal treatment by the coordination of trivalent iron and TPA as ligands, under an external magnetic field, to develop more efficient spintronic catalysts. As an efficient non-precious catalyst for OER under alkaline conditions, MIL-53(Fe–Ni)/NF-2200Gs electrode exhibited an ultralow overpotential of only 174 mV at 10 mA cm^{-2} and yielded large current densities at small overpotential (100 mA cm^{-2} at 235 mV and 1000 mA cm^{-2} at 319 mV) with the long-term durability. Moreover, the experimental results demonstrate that the excellent OER activity of MIL-53(Fe–Ni)/NF-2200Gs is closely related to its magnetic properties.

The well-shaped MIL-53(Fe–Ni)/NF-2200Gs were prepared on NF by a simple one-step process (Scheme 1). Owing to much higher $E_{Fe^{3+}/Fe^{2+}}^{\theta}$ (0.771 V) than $E_{Ni^{2+}/Ni}^{\theta}$ (−0.257 V), the Ni foam was redox-etched by Fe^{3+} and slowly released Ni^{2+} from the surface of the Ni foam, which results in the incorporation of Fe and Ni in MIL-53. To investigate the effects of magnetism, the samples under different intensities of external magnetic field (0, 2200Gs, and 4400Gs) were prepared. The details of the synthesis process are described in the Experimental section (ESI†). The powder X-ray diffraction (PXRD) patterns of MIL-53(Fe–Ni)/NF-

[a]College of Chemistry and Materials Science, Sichuan Normal University, Chengdu 610068, P. R. China. E-mail: xiefengyu@sicnu.edu.cn

[b]School of Chemistry and Chemical Engineering, Chongqing University, Chongqing 401331, P. R. China. E-mail: wenzeng@cqu.edu.cn

† Electronic supplementary information (ESI) available. See DOI: https://doi.org/10.1039/d2ra07666g
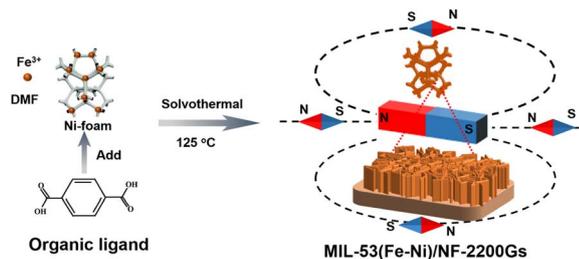
Scheme 1 Schematic diagram of the synthesis process of MIL-53(Fe–Ni)/NF-2200Gs.

2200Gs (Fig. S1a†) with the diffraction peaks at 8.9°, 11.4°, 15.6°, 18.7° and 20.8° are corresponding to the typical MIL-53 structure.[21,22] Compared with MIL-53(Fe–Ni)/NF-0 and MIL-53(Fe–Ni)/NF-4400Gs (Fig. 1a), their PXRD patterns were almost identical, indicating that the external magnetic field has no effect on the crystal type of the material. Subsequently, the thermogravimetric analysis data (Fig. 1b), Fourier transform infrared (FT-IR) spectroscopy (Fig. 1c), and Raman spectra (Fig. 1d) under external magnetic fields with different intensities were also presented. Assignments of the Raman peaks are based on previous data, wherein, peaks at 1437, 1610, 1138, 862, and 632 cm^{-1} are ascribed to the carboxylic acid groups and benzene ring in MIL-53.[23,24] The similar weight loss, FT-IR and Raman peaks suggested the external magnetic field made no difference to the crystal type, molecular structure, and surface functional groups of the material. SEM analysis showed that the entire surface of NF (Fig. 1e–g) was completely covered by MIL-53(Fe–Ni)/NF-2200Gs nanosheet arrays. The SEM images of MIL-53(Fe–Ni)/NF-0 and MIL-53(Fe–Ni)/NF-4400Gs are shown in Fig. S2 and S3,† respectively, which indicated that MIL-53(Fe–Ni) nanosheets became thinner under an external magnetic field. Fig. 1h presents the high-resolution TEM (HRTEM) image recorded on MIL-53(Fe–Ni)/NF-2200Gs that confirmed the

lattice fringes distance of 0.185 nm, matching well with the (110) plane of MIL-53.[25,26] The energy-dispersive X-ray (EDX) elemental mapping for MIL-53(Fe–Ni)/NF-2200Gs confirmed that Fe, Ni, C, and O elements were uniformly distributed on the whole nanoarray (Fig. 1i).

XPS analysis was then utilized to probe the surface chemistry of MIL-53(Fe–Ni)/NF-2200Gs. As shown in Fig. 2a, two fitted peaks located at 854.28 and 871.98 eV correspond to the BEs of Ni 2p$_{3/2}$ and Ni 2p$_{1/2}$, respectively, denoting the presence of Ni ions,[27] which showed that the oxidation state of Ni was +2 in MIL-53(Fe–Ni)/NF-2200Gs. In the Fe 2p region (Fig. 2b), the binding energies (BEs) at 707.28 and 711.88 eV can be attributed to Fe 2p$_{3/2}$, along with two peaks at 722.68 and 731.68 eV corresponding to Fe 2p$_{1/2}$, which indicated that Fe existed in the Fe^{2+} and Fe^{3+} valence state in MIL-53(Fe–Ni)/NF-2200Gs. Fig. 2d shows that the BE at 529.88 is assigned to the signals of O 1s.[28] The peaks at 282.98 and 286.78 eV are assigned to the C=C and O=C–OH of carboxylate ions in MIL-53(Fe–Ni)/NF-2200Gs,[29] respectively. These results illustrate that the MIL-53(Fe–Ni) nanosheet arrays were successfully formatted on the surface of NF.

Although the external magnetic field makes no difference to crystal type, molecular structure, and surface functional groups of the material, it makes a big difference to the electronic structure.

The OER performance of MIL-53(Fe–Ni)/NF-2200Gs with MIL-53(Fe–Ni)/NF-0 and MIL-53(Fe–Ni)/NF-4400Gs were further evaluated in 1.0 M KOH using a conventional three-electrode cell.[30] When current density reaches 10 mA cm^{-2},[31,32] the MIL-53(Fe–Ni)/NF-2200Gs requires an overpotential of 174 mV, while the activity of MIL-53(Fe–Ni)/NF-0 and MIL-53(Fe–Ni)/NF-4400Gs is worse, requiring an overpotential of 211 and 193 mV as shown in Fig. S7a.† More specifically, when the current density increases to 100 and 1000 mA cm^{-2}, the MIL-53(Fe–Ni)/NF-2200Gs only needs the overpotentials of 235 and 319 mV, respectively, while the other samples demand larger
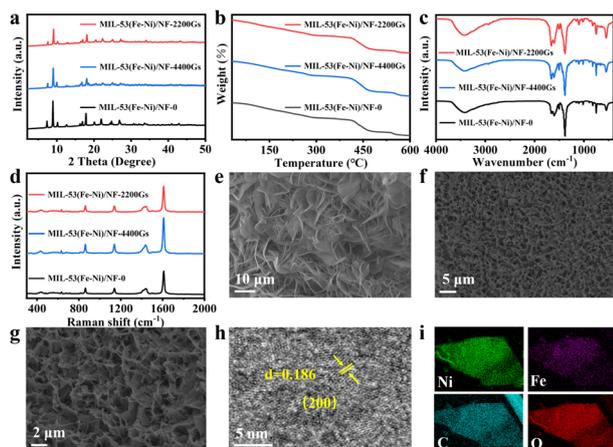

Fig. 1 Characterization of the MIL-53(Fe–Ni)/NF-2200Gs, MIL-53(Fe–Ni)/NF-4400Gs and MIL-53(Fe–Ni)/NF-0. (a) XRD pattern. (b) The thermal analysis image. (c) The FT-IR spectrum. (d) The Raman pattern. (e), (f) and (g) SEM images, (h) TEM image, and (i) Elemental mapping of Ni, Fe, C, and O elements for MIL-53(Fe–Ni)/NF-2200Gs.
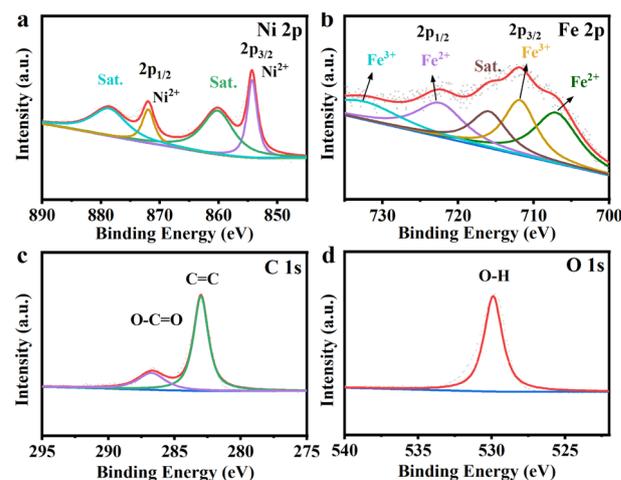

Fig. 2 Elemental XPS spectra of MIL-53(Fe–Ni)/NF-2200Gs, MIL-53(Fe–Ni)/NF-4400Gs, MIL-53(Fe–Ni)/NF-0 for Ni 2p (a), Fe 2p (b), C 1s (c) and O 1s (d).

overpotentials to approach the same current density (Fig. 3a). The MIL-53(Fe–Ni)/NF-2200Gs showed superior OER activity to different-stated non-noble-metal OER catalysts (more OER electrocatalyst are listed in Table S1†). To further understand the OER kinetics, Fig. 3b shows the Tafel slope obtained by linearly fitting the transformed polarization curves using the Tafel equation. We obtained the corresponding Tafel slope of MIL-53(Fe–Ni)/NF-2200Gs as 58 mV dec^{-1}, which is lower than the slope of MIL-53(Fe–Ni)/NF-0 (63 mV dec^{-1}) and MIL-53(Fe–Ni)/NF-4400Gs (84 mV dec^{-1}), indicating that the external magnetic field can reduce the kinetic barrier of MIL-53(Fe–Ni)/NF. From the electrochemical impedance spectroscopy (EIS) of the electrode kinetics, MIL-53(Fe–Ni)/NF-2200Gs demonstrates a lower charge transfer resistance than that of MIL-53(Fe–Ni)/NF-0 and MIL-53(Fe–Ni)/NF-4400Gs. The conductivity improvement implies that the electronic structure of MIL-53(Fe–Ni)/NF-2200Gs changed under the external magnetic field. Thus, the smallest Tafel slope and charge-transfer resistance of MIL-53(Fe–Ni)/NF-2200Gs implied the fastest reaction kinetics.

To identify the main factor to enhance the OER electrocatalytic activity, the potential factors were investigated one by one.

Potential factor 1

The electrochemically-active surface area was evaluated by measuring the double layer capacitance (C_{dl}) at the solid–liquid interface by the cyclic voltammetry (CV) method in Fig. 3. Fig. 3c and d show cyclic voltammetry (CV) plots of MIL-53(Fe–Ni)/NF-2200Gs and MIL-53(Fe–Ni)/NF-4400Gs,[33] respectively. Their linear relationships of current density *versus* scan rates at 1.23 V *vs.* RHE are shown in Fig. 3e and f. As a result, the C_{dl} values of MIL-53(Fe–Ni)/NF-0, MIL-53(Fe–Ni)/NF-2200Gs, and MIL-53(Fe–Ni)/NF-4400Gs were calculated, their linear relationships of current density *versus* scan rates were 4.34, 3.85, and 4.37 mF cm^{-2}, respectively, indicating that MIL-53(Fe–Ni)/NF-4400Gs

has a largest active surface area, in comparison with MIL-53(Fe–Ni)/NF-0 and MIL-53(Fe–Ni)/NF-2200Gs. The results strongly support that the specific surface area of MIL-53(Fe–Ni)/NF-2200Gs is not the main factor for OER activity.

Potential factor 2

As is known, the resulting electrode possessed a super-hydrophilic surface that could promote gas release and electrolyte transport, which is a key aspect that needs to be considered for designing high-current-density electrocatalysts.[34] The contact angles between MIL-53(Fe–Ni)/NF-0, MIL-53(Fe–Ni)/NF-2200Gs, and MIL-53(Fe–Ni)/NF-4400Gs with H_2O are 73°, 72°and 51°, respectively, which indicates their superhydrophilic properties, as shown in Fig. 4a–c. More attractively, under an external magnetic field, the surface hydrophilicity of MIL-53(Fe–Ni)/NF-2200Gs decreases significantly with respect to MIL-53(Fe–Ni)/NF-4400Gs, revealing that super hydrophilic is not the key factor for the catalytic activity.

Potential factor 3

The defect chemistry control of electrocatalysts endows the electrocatalysts with high intrinsic activity, thus significantly optimizing the OER performance. The oxygen vacancies (Ov) not only can effectively increase electrical conductivity but also can optimize the adsorption energy of reaction intermediates, which was proved to be highly efficient for OER. Electron paramagnetic resonance (EPR) spectroscopy is sensitive to Ov generation and concentration.[35,36] As can be seen from Fig. 4d, MIL-53(Fe–Ni)/NF-0 and MIL-53(Fe–Ni)/NF-4400Gs exhibit the remarkable stronger characteristic peak at $g = 2.007$, assigned to oxygen vacancies compared with MIL-53(Fe–Ni)/NF-2200Gs, indicating that MIL-53(Fe–Ni)/NF-0 and MIL-53(Fe–Ni)/NF-4400Gs have higher oxygen vacancy concentrations. As a result, it can be unambiguously concluded that the abundant oxygen vacancies are not the main factor for OER.
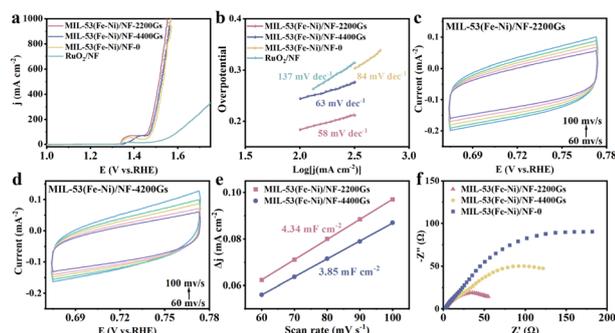

Fig. 3 Catalytic evaluation of MIL-53(Fe–Ni)/NF-2200Gs, MIL-53(Fe–Ni)/NF-4400Gs, MIL-53(Fe–Ni)/NF-0 and RuO_2/NF in 1.0 M KOH. (a) Polarization curves (b) Tafel slopes. (c) and (d) Cyclic voltammetry plots of MIL-53(Fe–Ni)/NF-2200Gs, MIL-53(Fe–Ni)/NF-4400Gs in 1 M KOH for the ECSA measurement. (e) Scan rates current plots of MIL-53(Fe–Ni)/NF-2200Gs and MIL-53(Fe–Ni)/NF-4400Gs obtained from the previous CV graph. (f) Nyquist plots.
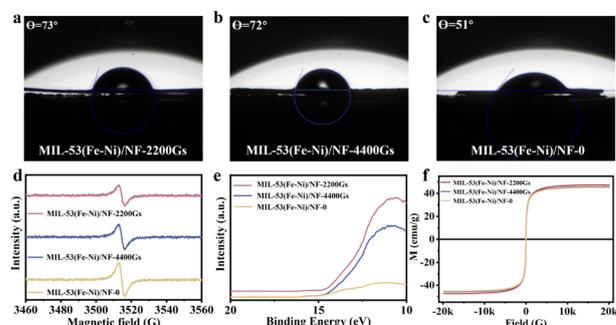

Fig. 4 Characterization of MIL-53(Fe–Ni)/NF-2200Gs, MIL-53(Fe–Ni)/NF-4400Gs and MIL-53(Fe–Ni)/NF-0. (a, b and c) contact angle measurements. (d) The EPR spectra (e) the UPS spectra. (f) Magnetic hysteresis curves.

Potential factor 4

Fig. S8† shows XPS spectra of MIL-53(Fe–Ni)/NF-2200Gs, MIL-53(Fe–Ni)/NF-0 and MIL-53(Fe–Ni)/NF-4400G electronic structures. Compared with the binding energy of MIL-53(Fe–Ni)/NF-0, the BEs of Ni 2p for MIL-53(Fe–Ni)/NF-2200Gs and MIL-53(Fe–Ni)/NF-4400Gs are positively shifted, while the peak of Fe $2p_{3/2}$ showed a negative shift and the peaks of Fe $2p_{1/2}$ showed a positive shift. The Fe 2p BE (707.28 eV) of MIL-53(Fe–Ni)/NF-2200Gs shifted to a higher binding energy compared to that in MIL-53(Fe–Ni)/NF-4400Gs. This suggests that Fe and Ni in MIL-53(Fe–Ni)/NF-2200Gs carry partial positive ($\delta-$) and negative ($\delta+$) charges, respectively, which result from electron transfer from Ni to Fe. The above results allow for faster charge-carrier transportation, which is consistent with the EIS. For a more in-depth analysis of the electronic structure, ultraviolet photoelectron spectroscopy (UPS) was conducted to investigate the work functions (φ) of the electrodes, as shown in Fig. 4e and S9.† Based on the formula $\varphi = hv - E_{\text{cutoff}}$,[38–40] the φ of MIL-53(Fe–Ni)/NF-0, MIL-53(Fe–Ni)/NF-2200Gs, and MIL-53(Fe–Ni)/NF-4400Gs were determined to be 14.67, 15.09, and 16.35 eV, respectively, suggesting that the electronic structure in Fe-MOF was slightly modified under the external magnetic field. Undoubtedly, lower φ corresponds to a higher electron transfer essence, thus demonstrating that MIL-53(Fe–Ni)/NF-22200Gs has the smallest energy barrier for electron transfer, which favors the improvement of OER activities. Moreover, lower φ corresponds to a higher Fermi energy level (E_F), illustrating that the d band center (E_d) energy level followed the order that 2200Gs > 4400Gs > 0Gs. According to the d-band theory, the moderate rise in E_d energy levels, which enhances the bond energy between the electrode and the adsorbed oxygen intermediates (*O, *OH, and *OOH), eventually leads to boosting of the OER activity. Based on the above analysis, the external magnetic field can successfully modify Fe-MOF, leading to a more excellent local electronic configuration, which is profitable for its intrinsic electrochemical activity. Meanwhile, the magnetic properties of MIL-53(Fe–Ni)/NF-2200Gs were measured by the magnetization *versus* magnetic field (M–H) curves (Fig. 4f and S10†), revealing that the synthesized materials have ferromagnetic properties.[41,42] The results show that MIL-53(Fe–Ni)/NF-2200Gs has the highest saturation value of $\approx$ 47.45 emu g^{-1} than that of MIL-53(Fe–Ni)/NF-4400Gs ($\approx$ 45.80 emu g^{-1}) and MIL-53(Fe–Ni)/NF-0 ($\approx$ 45.14 emu g^{-1}). According to the previous reports, electron spin polarization could enhance the catalytic activity of OER, because the unique OER steps from singlet reactant to the triplet product ($\uparrow$O=O$\uparrow$) call for a spin-selective electron transfer.[43–46] Furthermore, the Fe and Ni catalysts have excellent OER catalytic activity. It is worth noting here that Ni and Fe occupy different d-orbitals that determine the electron transfer rate and reaction thermodynamics, which are intrinsically dependent on the cation's spin state. An external magnetic field could improve the spin polarization in the catalysts, as such, it has a positive effect on the OER reaction. It can be seen from the experimental results that MIL-53(Fe–Ni)/NF-2200Gs has the strongest magnetic property

and the best OER catalytic activity. Thus, an external magnetic field enhances the magnetic properties of the catalyst, leading to the improvement of the spin polarization, which adjusts the d-electron results of the catalyst to optimize the kinetics of the OER reaction. An interesting finding is that the enhancement of OER performance was observed after the magnetization, which could be credited to the stable magnetization of the catalyst after the magnetic field was removed. This is because the induced spin alignment was still aligned in the magnetized Fe-MOF after removing the magnetic field. Besides, the MIL-53(Fe–Ni)/NF-2200Gs of the OER activity decreased with the prolongation of its heat treatment time (Fig. S11†), under that the magnetic domains in MIL-53(Fe–Ni)/NF-2200Gs became disordered by thermal disturbance. The above experimental results proved good OER activity of MIL-53(Fe–Ni)/NF-2200Gs, which was due to the increase in the external magnetic field increasing spin polarization and optimizing the d-electron configuration.

The turnover frequency (TOF) "widel" use in the molecular catalytic region can also be used for electrocatalytic reactions. TOF is defined as the number of conversions of a single active site per unit time and is related to the number of oxygen molecules produced per second in the OER. To calculate the TOF, we first measured the different scan rates of the CV of MIL-53(Fe–Ni)/NF-2200Gs (Fig. 5a) indicating a linear relationship between the oxidation peak current of the scan rate (Fig. 5b).[47,48] Then, we calculated a high TOF of 0.25 s^{-1} at the overpotential of 211 mV (Fig. 5c) according to the previously reported formula, which is higher than that previously reported for OER catalysts, including Co$_{1.8}$Ni-LDH (1.47 s^{-1}, η= 350 mV), Fe/Ni$_2$(OH)$_2$(L4) (0.3 s^{-1}, η = 300 mV), MSC-Ni$_{0.91}$Fe$_{0.09}$(OH)$_2$ (16.9 s^{-1}, η = 350 mV) and so on that are listed in Table S2.† Fig. 5d shows a multistep chronopotentiometric curve of MIL-53(Fe–Ni)/NF-2200Gs, the corresponding potential increases the current density from 30 to 250 mA cm^{-2} and remains constant for the next 500 seconds, reflecting outstanding transportation properties, conductivity, and mechanical properties of MIL-53(Fe–Ni)/NF-2200Gs.[49] In addition to OER activity, stability is another significant criterion for evaluating advanced
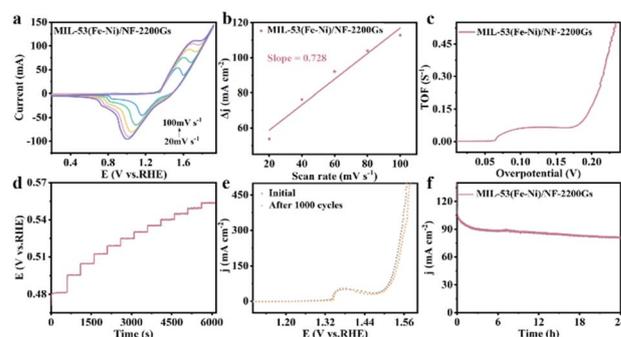

Fig. 5 Performance test of MIL-53(Fe–Ni)/NF-2200Gs. (a) CVs at different scan rates. (b) The plot of oxidation peak current *versus* the scan rate from CVs. (c) The calculated TOFs curves. (d) The multistep timing curve. (e) LSV curves of MIL-53(Fe–Ni)/NF-2200Gs before and after 1000 continuous chronoamperometry in 1.0 M KOH for OER. (f) Long-term stability test over 20 h.

© 2023 The Author(s). Published by the Royal Society of Chemistry

electrocatalysts. Hence, we tested MIL-53(Fe–Ni)/NF-2200Gs by successive cyclic voltammetry scanning. LSV curves exhibit that the loss is negligible compared to the initial cycle after 1000 cycles (Fig. 5e), reflecting its better stability. Remarkably, MIL-53(Fe–Ni)/NF-2200Gs showed excellent long-term stability, as confirmed by bulk electrolysis at a fixed current density of 205 mA cm^{-2}, demonstrating that MIL-53(Fe–Ni)/NF-2200Gs kept it active for at least 24 h (Fig. 5f). Subsequently, we measured FT-IR spectra of MIL-53(Fe–Ni)/NF-2200Gs before and after the stability test, as shown in Fig. S12.† The structure of the material is basically well maintained after OER, showing excellent structural stability. Thus, the preparation of MIL-53(Fe–Ni)/NF-2200Gs under an applied magnetic field is beneficial for mitigating the electrochemical reconstructing-induced stability loss and enhancing the catalytic performance. The mechanism of OER could be assigned to the existence of the two pairs of redox peaks in Fig. S13.† The testing results showed that the Fe sites served as the active sites in MIL-53(Fe–Ni)/NF-2200Gs.[50] In order to evaluate the intrinsic catalytic performance of MIL-53(Fe–Ni)/NF-2200Gs, we obtained the LSV curve normalized by ECSAs determined from the electrochemical experiments (Fig. S14†). Notably, MIL-53(Fe–Ni)/NF-2200Gs only required a minimum overpotential of 200 mV to reach the normalized current density of 1 mA cm^{-2} (Table S3†), confirming its significant intrinsic activity. As shown in Fig. S15,† after the OER cycle, the peak assigned to Fe^{3+} (appearing at 713.38 eV) increased. This is related to the conversion of Fe^{2+} to FeOOH during the oxidation of water.[37]

In conclusion, the MIL-53(Fe–Ni)/NF-2200Gs as an efficient and stable electrocatalyst for the oxygen-evolution reaction in alkaline media was obtained via a one-pot hydrothermal method under an external magnetic field. Compared with MIL-53(Fe–Ni)/NF-0 and MIL-53(Fe–Ni)/NF-4400Gs, the MIL-53(Fe–Ni)/NF-2200Gs exhibited superior performance and achieved a low overpotential of 174 mV at 10 mA cm^{-2}. Meanwhile, the improvement in the catalytic activity can be attributed to the enhanced electron spin polarization and optimized d-orbital configuration of metal ions under external magnetic fields, which are confirmed by ultraviolet photoelectron spectroscopy and electrochemical measurements. This work not only establishes a series of transition-metal-based ferromagnetic electrocatalysts but also provides a new insight from the point view of the external magnetic field into the further rational designing and modulation of OER electrocatalytic materials.

Conflicts of interest

There are no conflicts to declare.

Acknowledgements

Notes and references

1 J. Song, C. Wei, Z. F. Huang, C. Liu, L. Zeng, X. Wang and Z. J. Xu, *Chem. Soc. Rev.*, 2020, **49**, 2196–2214.

2 N. T. Suen, S. F. Hung, Q. Quan, N. Zhang, Y. J. Xu and H. M. Chen, *Chem. Soc. Rev.*, 2017, **46**, 337–365.

3 K. Zeng and D. Zhang, *Prog. Energy Combust. Sci.*, 2010, **36**, 307–326.

4 H. Jiang, J. Gu, X. Zheng, M. Liu, X. Qiu, L. Wang, W. Li, Z. Chen, X. Ji and J. Li, *Energy Environ. Sci.*, 2019, **12**, 322–333.

5 L. C. Seitz, C. F. Dickens, K. Nishio, Y. Hikita, J. Montoya, A. Doyle, C. Kirk, A. Vojvodic, H. Y. Hwang, J. K. Norskov and T. F. Jaramillo, *Science*, 2016, **353**, 1011–1014.

6 T. Schuler, T. Kimura, T. J. Schmidt and F. N. Büchi, *Energy Environ. Sci.*, 2020, **13**, 2153–2166.

7 T. Lim, J. W. H. Niemantsverdriet and J. Gracia, *ChemCatChem*, 2016, **8**, 1–8.

8 J. Gracia, R. Sharpe and J. Munarriz, *J. Catal.*, 2018, **361**, 331–338.

9 T. Wu and Z. J. Xu, *Curr. Opin. Electrochem.*, 2021, **30**, 100804.

10 G. Chen, Y. Sun, R. R. Chen, C. Biz, A. C. Fisher, M. P. Sherburne, J. W. Ager Iii, J. Gracia and Z. J. Xu, *JPhys Energy*, 2021, **3**, 031004.

11 J. Gracia, J. Munarriz, V. Polo, R. Sharpe, Y. Jiao, J. W. H. Niemantsverdriet and T. Lim, *ChemCatChem*, 2017, **9**, 3358–3363.

12 J. Gracia, *Phys. Chem. Chem. Phys.*, 2017, **19**, 20451–20456.

13 Y. Sun, J. Wang, Q. Liu, M. Xia, Y. Tang, F. Gao, Y. Hou, J. Tse and Y. Zhao, *J. Mater. Chem. A*, 2019, **7**, 27175–27185.

14 F. A. Garcés-Pineda, M. Blasco-Ahicart, D. Nieto-Castro, N. López and J. R. Galán-Mascarós, *Nat. Energy*, 2019, **4**, 519–525.

15 J. Gracia, C. Biz and M. Fianchini, *Mater. Today Commun.*, 2020, **23**, 100894.

16 C. C. Mayorga-Martinez, Z. Sofer, D. Sedmidubsky, S. Huber, A. Y. Eng and M. Pumera, *ACS Appl. Mater. Interfaces*, 2017, **9**, 12563–12573.

17 Y. Ma, G.-M. Mu, Y.-J. Miao, D.-M. Lin, C.-G. Xu, F.-Y. Xie and W. Zeng, *Rare Met.*, 2021, **41**, 844–850.

18 G. Mu, Y. Miao, M. Wu, Q. Xiang, D. Lin, C. Xu and F. Xie, *J. Electrochem. Soc.*, 2021, **168**, 126508.

19 C.-P. Wang, Y. Feng, H. Sun, Y. Wang, J. Yin, Z. Yao, X.-H. Bu and J. Zhu, *ACS Catal.*, 2021, **11**, 7132–7143.

20 Z. Zhang, C. Wang, X. Ma, F. Liu, H. Xiao, J. Zhang, Z. Lin and Z. Hao, *Small*, 2021, **17**, 2103785.

21 C. Rodriguez Correa, M. Bernardo, R. P. P. L. Ribeiro, I. A. A. C. Esteves and A. Kruse, *J. Anal. Appl. Pyrolysis*, 2017, **124**, 461–474.

22 H. Chen, Y. Liu, T. Cai, W. Dong, L. Tang, X. Xia, L. Wang and T. Li, *ACS Appl. Mater. Interfaces*, 2019, **11**, 28791–28800.

23 S. Bordiga, C. Lamberti, G. Ricchiardi, L. Regli, F. Bonino, A. Damin, K. P. Lillerud, M. Bjorgen and A. Zecchina, *Chem. Commun.*, 2004, **20**, 2300–2301.

24 M. W. Louie and A. T. Bell, *J. Am. Chem. Soc.*, 2013, **135**, 12329–12337.

25 C. Cao, D. D. Ma, Q. Xu, X. T. Wu and Q. L. Zhu, *Adv. Funct. Mater.*, 2018, **29**, 1807418.

26 F. Sun, G. Wang, Y. Ding, C. Wang, B. Yuan and Y. Lin, *Adv. Energy Mater.*, 2018, **8**, 1800584.

27 M. Liu, L. Kong, X. Wang, J. He and X. H. Bu, *Small*, 2019, **15**, 1903410.

28 Q. Qian, Y. Li, Y. Liu, L. Yu and G. Zhang, *Adv. Mater.*, 2019, **31**, 1901139.

29 V. Chandra, J. Park, Y. Chun, J. W. Lee, I. C. Hwang and K. S. Kim, *ACS Nano*, 2010, **4**, 3979–3986.

30 Y. Gou, L. Yang, Z. Liu, A. M. Asiri, J. Hu and X. Sun, *Inorg. Chem.*, 2018, **57**, 1220–1225.

31 S. F. Zai, X. Y. Gao, C. C. Yang and Q. Jiang, *Adv. Energy Mater.*, 2021, **11**, 2101266.

32 Y. Yang, H. Yao, Z. Yu, S. M. Islam, H. He, M. Yuan, Y. Yue, K. Xu, W. Hao, G. Sun, H. Li, S. Ma, P. Zapol and M. G. Kanatzidis, *J. Am. Chem. Soc.*, 2019, **141**, 10417–10430.

33 F. Wu, X. Guo, G. Hao, Y. Hu and W. Jiang, *Nanoscale*, 2019, **11**, 14785–14792.

34 J. Li, Y. Zhu, W. Chen, Z. Lu, J. Xu, A. Pei, Y. Peng, X. Zheng, Z. Zhang, S. Chu and Y. Cui, *Joule*, 2019, **3**, 557–569.

35 J. Huang, Y. Xiong, Z. Peng, L. Chen, L. Wang, Y. Xu, L. Tan, K. Yuan and Y. Chen, *ACS Nano*, 2020, **14**, 14201–14211.

36 F. Xiang, X. Zhou, X. Yue, Q. Hu, Q. Zheng and D. Lin, *Electrochim. Acta*, 2021, **379**, 138178.

37 M. Xie, Y. Ma, D. Lin, C. Xu, F. Xie and W. Zeng, *Nanoscale*, 2020, **12**, 67–71.

38 K. Kang, S. Watanabe, K. Broch, A. Sepe, A. Brown, I. Nasrallah, M. Nikolka, Z. Fei, M. Heeney, D. Matsumoto, K. Marumoto, H. Tanaka, S. Kuroda and H. Sirringhaus, *Nat. Mater.*, 2016, **15**, 896–902.

39 W. Chen, Y. Zhou, L. Wang, Y. Wu, B. Tu, B. Yu, F. Liu, H. W. Tam, G. Wang, A. B. Djurisic, L. Huang and Z. He, *Adv. Mater.*, 2018, **30**, 1800515.

40 J. Li, Z. Li, X. Liu, C. Li, Y. Zheng, K. W. K. Yeung, Z. Cui, Y. Liang, S. Zhu, W. Hu, Y. Qi, T. Zhang, X. Wang and S. Wu, *Nat. Commun.*, 2021, **12**, 1224.

41 X. Lai, G. Zhang, L. Zeng, X. Xiao, J. Peng, P. Guo, W. Zhang and W. Lai, *ACS Appl. Mater. Interfaces*, 2021, **13**, 1413–1423.

42 M. Takeuchi, M. Suzuki, S. Kobayashi, Y. Kotani, T. Nakamura, N. Kikuchi, A. Bolyachkin, H. Sepehri-Amin, T. Ohkubo, K. Hono, Y. Une and S. Okamoto, *NPG Asia Mater.*, 2022, **14**, 70.

43 A. B. Urgunde, G. Bahuguna, A. Dhamija, V. Kamboj and R. Gupta, *Mater. Res. Bull.*, 2021, **142**, 111380.

44 Y. Li, T. Wang, M. Asim, L. Pan, R. Zhang, Z.-F. Huang, Z. Chen, C. Shi, X. Zhang and J.-J. Zou, *Trans. Tianjin Univ.*, 2022, **28**, 163–173.

45 H. B. Zheng, Y. L. Wang, J. W. Xie, P. Z. Gao, D. Y. Li, E. V. Rebrov, H. Qin, X. P. Liu and H. N. Xiao, *ACS Appl. Mater. Interfaces*, 2022, **14**, 34627–34636.

46 X. Ren, T. Wu, Y. Sun, Y. Li, G. Xian, X. Liu, C. Shen, J. Gracia, H. J. Gao, H. Yang and Z. J. Xu, *Nat. Commun.*, 2021, **12**, 2608.

47 W. Hu, Q. Liu, T. Lv, F. Zhou and Y. Zhong, *Electrochim. Acta*, 2021, **381**, 138276.

48 Z. Wang, J. Xu, J. Yang, Y. Xue and L. Dai, *Chem. Eng. J.*, 2022, **427**, 131498.

49 H. Zhang, X. Li, A. Hähnel, V. Naumann, C. Lin, S. Azimi, S. L. Schweizer, A. W. Maijenburg and R. B. Wehrspohn, *Adv. Funct. Mater.*, 2018, **28**, 1706847.

50 J. N. Tiwari, N. K. Dang, S. Sultan, P. Thangavel, H. Y. Jeong and K. S. Kim, *Nat. Sustain.*, 2020, **3**, 556–563.